MULTI-NEEDLE LOCALIZATION FOR PELVIC SEED IMPLANT BRACHYTHERAPY BASED ON TIP-HANDLE DETECTION AND MATCHING

Zhuo Xiao¹, Fugen Zhou¹, Jingjing Wang¹, Chongyu He¹, Bo Liu¹, Haitao Sun², Zhe Ji², Yuliang Jiang², Junjie Wang², and Oiuwen Wu³

¹Image Processing Center, Beihang University, Beijing 100191, China ²Department of Radiation Oncology, Peking University Third Hospital, Beijing 100191, China ³Department of Radiation Oncology, Duke University Medical Center, Durham, NC 27710, USA bo.liu@buaa.edu.cn

ABSTRACT

Accurate multi-needle localization in intraoperative CT images is crucial for optimizing seed placement in pelvic seed implant brachytherapy. However, this task is challenging due to poor image contrast and needle adhesion. This paper presents a novel approach that reframes needle localization as a tip-handle detection and matching problem to overcome these difficulties. An anchor-free network, based on HRNet, is proposed to extract multi-scale features and accurately detect needle tips and handles by predicting their centers and orientations using decoupled branches for heatmap regression and polar angle prediction. To associate detected tips and handles into individual needles, a greedy matching and merging (GMM) method designed to solve the unbalanced assignment problem with constraints (UAP-C) is presented. The GMM method iteratively selects the most probable tip-handle pairs and merges them based on a distance metric to reconstruct 3D needle paths. Evaluated on a dataset of 100 patients, the proposed method demonstrates superior performance, achieving higher precision and F1 score compared to a segmentation-based method utilizing the nnUNet model, thereby offering a more robust and accurate solution for needle localization in complex clinical scenarios.

Keywords: Multi-needle localization, Object detection, CT images, Unbalanced assignment problem with constraints, Brachytherapy.

1 Introduction

Colorectal cancer ranks 3rd in the global incidence of malignant tumors and 2nd in mortality [1]. Brachytherapy, leveraging its capacity for highly localized dose delivery and superior radiobiological effects, has been successfully used to treat this disease [2,3]. A key factor in the efficacy of Seed Implant Brachytherapy (SIBT) is the precise delivery of a sufficient radiation dose to the target area while minimizing exposure to organs at risk (OARs). To achieve optimal dose distribution, SIBT involves preoperatively determining needle paths and seed positions, followed by needle insertion. Intraoperative planning is then performed using CT images acquired post-insertion [4–6].

Accurate localization of the implanted needles is crucial during this process to optimize seed placement. The actual needle positions frequently deviate from the pre-operative plan due to factors such as organ deformation and tissue resistance. In current clinical practice, physicians primarily perform this localization manually, a process that is time-consuming, labor-intensive, and heavily reliant on experience.

Extracting needle paths from CT images is challenging due to the partial-volume effect. This results in uneven and obscure grayscale distribution along the needle path, complicating both manual annotation and automatic segmentation, as shown in Fig.1(a1) and (a2). Additionally, needle adhesion makes it difficult to separate individual needle (Fig.1(b)). Furthermore, surrounding bone structures and previously-implanted seeds in cases of recurrent rectal cancer can have a significant impact on needle path localization (Fig.1(c)).

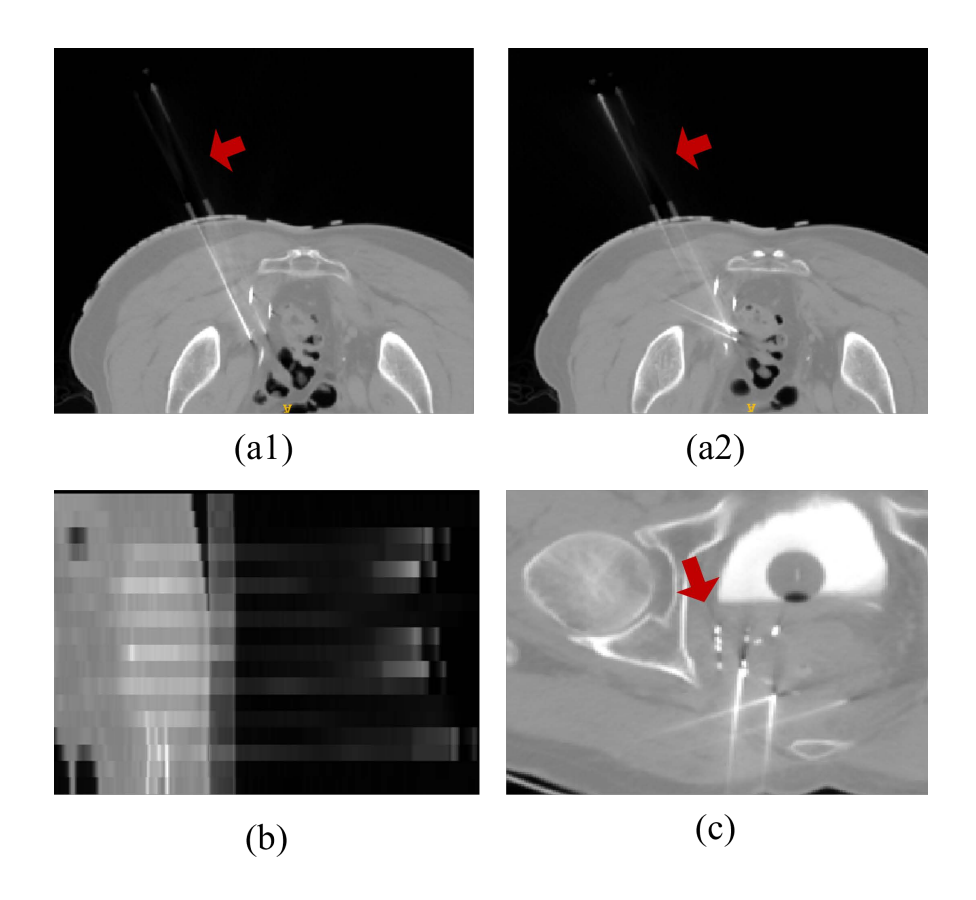


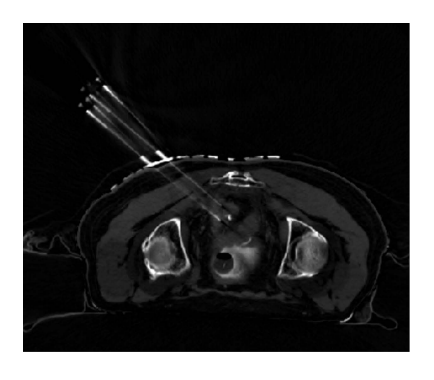
Figure 1: Challenges for multi-needle localization on CT. (a1)&(a2) The needle path indicated by the red arrow has very poor contrast in two consecutive axial slices. (b) Adhesion between needle paths in a sagittal slice. (c) Interference caused by previously-implanted seeds in CTs of recurrent rectal cancer cases.

While many studies have explored automatic needle localization, a significant gap remains in addressing the combined challenges of poor grayscale contrast and needle adhesion in complex multi-needle scenarios. Existing literature often focuses on perineal cranial to caudal needle trajectories, which are common in prostate and gynecological HDR-brachytherapy or biopsy procedures [7–15]. In contrast, transperitoneal needle trajectories pose greater challenges for automatic localization. Moreover, many previous studies concentrate on single-needle detection, which is inherently less challenging than accurate localization in dense multi-needle settings [7,16–19]. For lung seed implantation, Zhang et al. proposed a method combining thresholding and an improved RANSAC algorithm to extract and identify needle paths [20]. However, this approach is confined on 2D slice with significant limitations.

Among existing methods, segmentation-based approaches are the most promising for multi-needle localization in pelvic SIBT. These methods typically involve segmenting needles using traditional thresholding or deep learning, followed by post-processing to identify needle trajectory instances [20]. However, applying the segmentation-based method to the intraoperative brachytherapy CT remains challenging, as shown in Fig.2, which illustrates the insufficient segmentation results obtained with both conventional thresholding [21] and deep learning techniques [22, 23]. Furthermore, even with optimal segmentation, accurately extracting individual needle paths still remains difficult using traditional post-processing methods, such as curve fitting or connected component analysis due to the adhesion between needle paths.

Given these challenges, a deeper understanding of needle trajectory characteristics in CT images is essential. We observed that the needle handle, with its high contrast and visibility due to minimal external interference, provides a reliable reference. Similarly, the abrupt grayscale variations caused by metal artifacts [24] at the needle tip provide a distinct feature that can be leveraged for precise needle path localization.

To address the multi-needle localization problem, we propose a two-step approach: First, a tip-handle detection network is developed to detect needle tips and handles on axial slices. This network comprises a backbone for high-level semantic feature extraction and three anchor-free detection heads for tip-handle heatmap, local offset, and needle







(b) Threshold segmentation



(c) Deep learningbased segmentation

Figure 2: Demonstration of the insufficiency in segmentation results from both conventional thresholding and deep learning techniques. (a) One original axial CT slice. (b) Segmentation results using Otsu threshold [21]. (c) Segmentation results using deep learning-based method [23].

angle prediction. Second, the detected 2D tips and handles are matched to determine the 3D positions of needle tips and handles, and subsequently, the linear 3D needle paths. The matching problem is formulated as an unbalanced assignment problem with constraints (UAP-C), which we solve using a greedy matching and merging (GMM) method. This method is, to our knowledge, the first of its kind applied to multi-needle localization.

In summary, the contributions of this paper are as follows:

- We pioneer a new paradigm for multi-needle localization by reframing it as a tip-handle detection and matching problem, which involves detecting needle tips and handles and pairing them accurately.
- We develop an anchor-free detection network, which predict the centers and orientations of tips and handles through decoupled branches for heatmap regression and polar angle prediction.
- We introduce a greedy matching and merging method to solve the unbalanced assignment problem with constraints, iteratively selecting the most probable tip-handle pairs and merging them based on a distance metric to reconstruct individual needles.
- We annotated tips, handles, and needle paths in an intra-operation CT dataset of 100 patients, and experimental results demonstrate that our approach outperforms segmentation-based methods in precision and recall while achieving comparable accuracy in localization and orientation.

2 Related Works

2.1 Object detection

Object detection aims to identify and classify objects within an image. In recent years, deep learning-based methods have dominated this field, primarily categorized into CNN-based and transformer-based approaches [25]. CNN-based object detection can be further divided into two-stage [26] and one-stage [27–30] methods. Two-stage detectors first generate region proposals [26] and then classify and refine their positions, ensuring high accuracy. One-stage detectors, on the other hand, bypass the proposal step and directly predict object locations and categories in a single pass, making them faster but sometimes less precise. DETR (Detection transformer) [31] revolutionizes object detection by treating it as a set prediction problem, which employs a transformer encoder-decoder architecture to directly predict object classes and bounding boxes in one step. However, DETR models typically require a large amount of training data and tend to converge slowly, making them less suitable for scenarios with limited data or real-time applications. This is particularly relevant in medical imaging datasets, which are typically much smaller in scale compared to those used for natural scenes. Therefore, our method adopts a CNN-based approach, which is more efficient in data-limited settings. Furthermore, in our case, the needle tips and handles have relatively fixed sizes, meaning that detecting their center points and orientations is more relevant than bounding boxes. To achieve this, we propose an anchor-free network that incorporates an angle prediction branch to fit the characteristics of the task.

2.2 Assignment problem

The assignment problem (AP) is a core combinatorial optimization challenge, seeking to optimize the allocation of tasks to agents on a one-to-one basis, typically by minimizing total cost or maximizing total benefit. For standard, small-scale AP instances, established algorithms such as the Hungarian algorithm [32] and linear programming [33] provide optimal solutions. However, the generalized assignment problem(GAP) [34] introduces resource constraints, such as agent capacities [35], making the problem NP-hard. Consequently, heuristic [36, 37] and metaheuristic [38] approaches are frequently employed for practical, large-scale applications. More recently, machine learning [39] and reinforcement learning [40] have emerged as promising tools for tackling complex assignment problems, offering adaptive and efficient solutions in domains such as the Weapon-Target Assignment (WTA) problem [41] and the Multi-Resource Generalized Assignment (MRGA) problem [42]. Nevertheless, these learning-based methods often lack rigorous theoretical performance guarantees and necessitate substantial training time, posing limitations in scenarios requiring rapid deployment or real-time responsiveness.

3 Methods

3.1 Overview

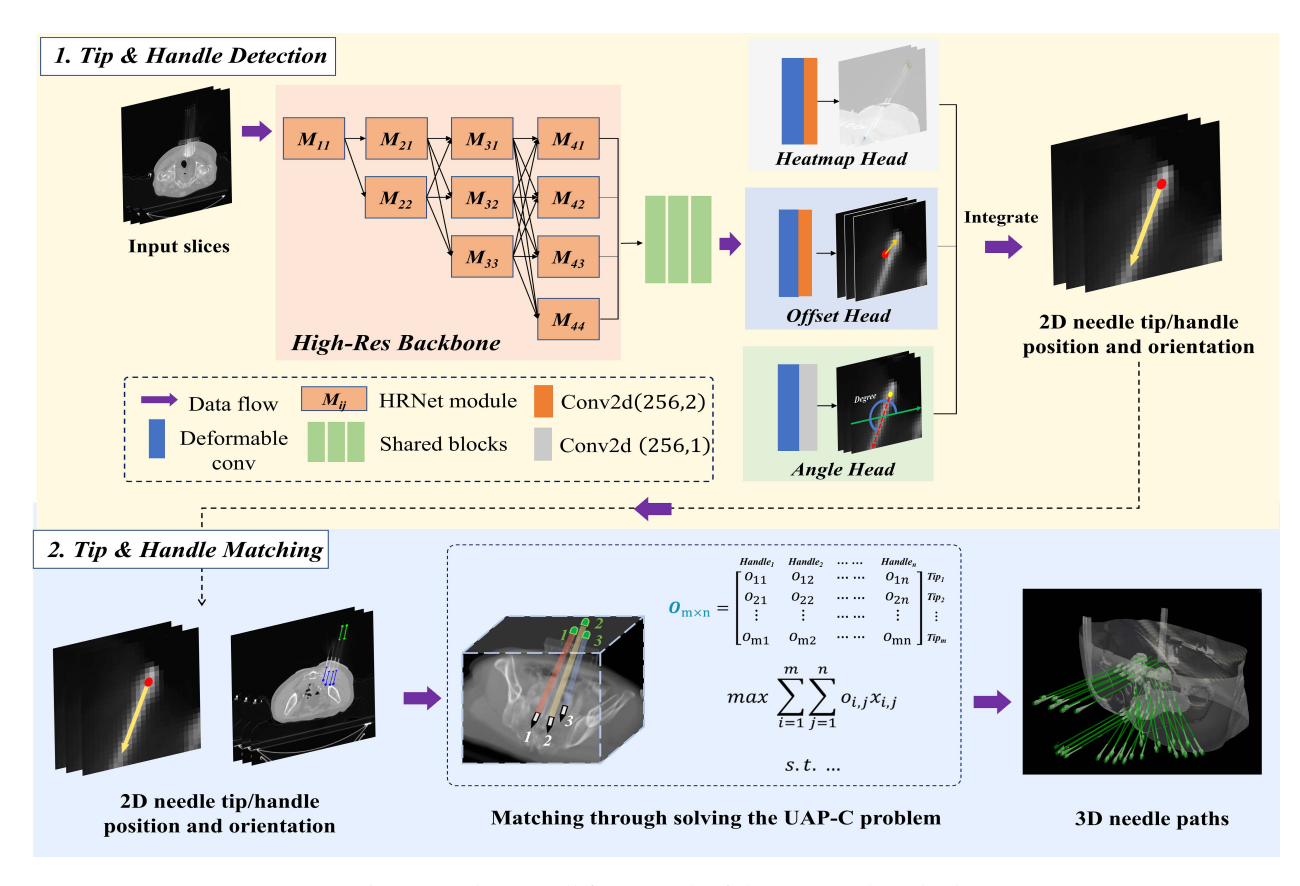


Figure 3: The overall framework of the proposed method

Fig. 3 illustrates the overall framework of the proposed method which consists of a tip-handle detection module and a tip-handle matching module. The detection module is designed to detect the needle tips and handles in 2D axial slices. It extracts multi-scale features through a high-resolution encoder, and predict the position of the needle tips and handles on the 2D axial slices through three prediction heads, including the heatmap head, the offset head, and the angle head. Based on the detection results, the tip-handle matching module match the detected tips and handles to determine the 3D needle path. The matching is formulated as an unbalanced assignment problem with constraints and a greedy matching and merging solving method is proposed to solve it.

For the tip-handle detection, the proposed detection framework uses a high-resolution backbone to extract multi-scale features, which are concatenated, processed through shared blocks, and then fed into three prediction heads (the

heatmap head, the offset head, and the angle head). The heatmap head predicts a 2-channel heatmap that represents the probability of a pixel being the needle tip and handle. Local maxima within the 8-neighborhood of each pixel in the heatmap are then searched and those local maxima whose values exceed a predefined threshold are considered center point candidates for tips and handles. The offset head predicts an offset vector $(\Delta x, \Delta y)$ to compensate for quantization errors between the input image and the down-sampled heatmap resolution, ensuring more precise localization of the center points. The angle head predicts a polar angle θ for each pixel, which represents the 2D orientation of the needle related to the detected tip and handle in axial slices. This angle is defined as the direction of the vector connecting the tip or handle to the opposite end, measured relative to the X-axis, within the range $[0,2\pi)$. Detection is performed in 2D manner across all CT slices, and by integrating the results from three heads, the 3D positions (x_o, y_o, z_o) and orientation α_o of the objects are determined.

Based on the predicted information of needle tip and handle, all possible pairs of needle tips and handles are established. By incorporating a priori constraints and an objective function, an UAP-C is formulated. The proposed tip-handle matching strategy then applied to merge duplicates and pair each needle tip with its corresponding needle, ensuring precise localization of 3D needle instances. The detailed process of matching strategy will be described in subsequent sections.

3.2 Detection of needle tips and handles

3.2.1 Network architecture

The tip-handle detection network comprises of a feature extractor and three output heads. The feature extractor uses HRNet [43] as backbone, which excels at preserving high-resolution details, making it particularly effective for detecting small target objects like needle tips and handles. After extracting multi-scale features through the backbone network, low-resolution feature maps are up-sampled to align with high-resolution feature maps and concatenated together, which are then fed into three convolutional blocks. The convolutional blocks are shared for the following three output heads, designed to minimize network redundancy and complexity while maintaining detection accuracy. Each convolutional block consists of a convolutional layer, a batch normalization layer, and a ReLU activation function, with the convolutional layer using a 3×3 kernel.

The output features of the shared convolutional blocks are passed to three distinct output heads, each responsible for different tasks: a heatmap prediction head for handles and tips, a local offset head, and a target angle prediction head. Since the sizes of the needle handles and tips are fixed and not the primary focus of this study, the size branch is dropped, which typically predicts object dimensions in traditional detection frameworks [28, 44, 45]. The radii of the needle tip and handle were set to 4 mm and 3 mm, respectively, at the input image scale for heatmap generation.

Each head consists of a deformable convolution [46] and a standard 3×3 convolution. Unlike regular convolutions that operate on a fixed spatial grid, deformable convolutions dynamically adjust their sampling points, enabling adaptive and flexible feature extraction. Specifically, in a regular 3×3 convolution, the 9 sampling locations are fixed. In deformable convolutions, the positions of these sampling points are shifted by learned offsets $\Delta \mathbf{p} = (\Delta x, \Delta y)$, allowing the convolution to adapt to the object's geometry and capture more relevant features.

3.2.2 Loss function

To train our detection network, a multi-task loss function is designed which is comprised of three items:

$$L_{\text{det}} = \lambda_{\text{HM}} L_{\text{HM}} + \lambda_{\text{off}} L_{\text{off}} + \lambda_{\text{ang}} L_{\text{ang}}$$
(1)

where $L_{\rm HM}$ is the heatmap loss, $L_{\rm off}$ is the offset loss, and $L_{\rm ang}$ is the angle prediction loss. $\lambda_{\rm HM}$, $\lambda_{\rm off}$, and $\lambda_{\rm ang}$ are the weighting factors for each loss term, respectively.

The ground truth of heatmap for needle tip and handle is calculated based on a 2D Gaussian kernel centered at the manually picked center points of the tips or handles. Focal Loss [47] is adopted to optimize the pixel-level logistic regression of heatmap:

$$L_{\text{HM}} = \frac{-1}{N} \sum_{(x,y,c)} \begin{cases} P_{(x,y)}^c & \text{if } H_{(x,y)}^c = 1\\ Q_{(x,y)}^c & \text{otherwise} \end{cases}$$
 (2)

where $P^c_{(x,y)}=(1-\hat{H}^c_{(x,y)})^{\alpha}\log(\hat{H}^c_{(x,y)}), \ Q^c_{(x,y)}=(1-H^c_{(x,y)})^{\beta}(\hat{H}^c_{(x,y)})^{\alpha}\log(1-\hat{H}^c_{(x,y)}), \ \hat{H}^c_{(x,y)}$ denotes the predicted value at pixel (x,y) for class $c,H^c_{(x,y)}$ is the ground truth value, α and β are weighting hyper-parameters, and N is the number of key points.

The offset layer is intended to correct the position inaccuracies after down sampling. The center location (x, y) in the original image is mapped to the location $(\lfloor \frac{x}{d} \rfloor, \lfloor \frac{y}{d} \rfloor)$ in the heatmaps, where d is the down-sampling factor. The offset o_k and offset loss L_{off} are defined as follows:

$$o_k = \left(\frac{x_k}{d} - \left\lfloor \frac{x_k}{d} \right\rfloor, \frac{y_k}{d} - \left\lfloor \frac{y_k}{d} \right\rfloor\right) \tag{3}$$

$$L_{\text{off}} = \frac{1}{N} \sum_{k=1}^{N} \text{Smooth}_{L1}(o_k, \hat{o}_k)$$

$$\tag{4}$$

where smooth L1 loss is given by:

$$Smooth_{L1}(x_i, y_i) = \begin{cases} 0.5(x_i - y_i)^2 & \text{if } |x_i - y_i| < 1\\ |x_i - y_i| - 0.5 & \text{otherwise} \end{cases}$$
 (5)

The final loss is used to regress the 2D orientation of tips and handles, predicting the polar angle at each pixel location in the heatmap. Due to the periodic nature of angles [48], applying an L1 loss directly to the angle predictions is impractical, as it would introduce discontinuities at angular boundaries. Instead, a cosine loss is employed to address this periodicity:

$$L_{\text{ang}} = \frac{1}{N} \sum_{k=1}^{N} \left(1 - \cos(\hat{\theta}_k - \theta_k) \right) \tag{6}$$

Here, θ_k is the ground truth angle for the k-th object, and $\hat{\theta}_k$ is the predicted angle.

3.3 Matching of needle tips and handles

After utilizing detection networks to identify the 2D positions and orientations of needle handles and tips across all slices, a tip-handle matching algorithm is proposed to match the corresponding handles and tips to determine the 3D needle paths. We formulate the problem as an unbalanced assignment problem with constraints and propose to solve it through a greedy matching and merging method.

3.3.1 The unbalanced assignment problem with constraints

The assignment problem is a fundamental combinatorial optimization problem that involves assigning an equal number of tasks to agents, with the goal of minimizing total cost or maximizing total benefit. The UAP-C extends the assignment problem, where the number of tasks and agents may not be equal, and the number of possible matchings may be less than the number of tasks and agents. Furthermore, additional constraints are imposed during the assignment process. In the context of our problem, the tasks represent needle tips, while the agents are needle handles. Table 1 presents the notation used in the UAP-C model for the tip-handle matching problem.

Using these definitions, the tip-handle matching problem can be mathematically formulated as follows:

$$\max \sum_{i=1}^{m} \sum_{j=1}^{n} o_{i,j} x_{i,j} \tag{7}$$

s.t.
$$\sum_{i \in T} x_{i,j} \le 1 \quad \forall j \in H$$
 (8)

$$\sum_{i \in H} x_{i,j} \le 1 \quad \forall i \in T \tag{9}$$

$$|L_{i,j} - L_{\text{prior}}| < \varepsilon_l \quad \forall i \in T, j \in H$$
 (10)

$$|\mathbf{at}_i - \mathbf{ah}_j| < \varepsilon_a \quad \forall i \in T, j \in H$$
 (11)

NoCross
$$(i, j, k, l)$$
 $\forall i, k \in T, j, l \in H, i \neq k, j \neq l$ (12)

$$x_{i,j} \in \{0,1\} \quad \forall i \in T, j \in H \tag{13}$$

$$\sum_{i=1}^{m} \sum_{j=1}^{n} x_{i,j} = N_{\text{prior}}$$
 (14)

In this model, the objective is to maximize the total score of all matched tip-handle pairs. Considering that the HU value along the needle path is relatively high, we propose to define the score function based on the analysis of the statistics of

Table 1: The description of sets.		- d : 4l 4: l	dl = 4 - le : le l =
Table 1. The describition of sets	narameters and variables its	ea in ine iin-nan	ale maiching broblem
Table 1. The description of sets,	parameters, and variables as	ca in the tip nan	are matering problem.

Function / Symbol	Description
NoCross	No two needles in the solution set intersect, which can be checked using the shortest distance between two line segments.
Sets	
T	Set of detected needle tips, ranging from 1 to m
<i>H</i>	Set of detected needle handles, ranging from 1 to n
Parameters	
$o_{i,j}$	Score value for pairing tip i and handle j
$L_{i,j}$	3D Euclidean distance between the tip i and handle j (mm)
$L_{ ext{prior}}$ $arepsilon_l$	Pre-known needle length (mm) Tolerance for needle length difference (mm)
at_i	Detected angle for tip i (°)
ah_j	Detected angle for handle j (°)
$arepsilon_a$	Tolerance for angle difference (°)
$N_{ m prior}$	A priori number of implanted needles
Variable	
$x_{i,j}$	1 if tip i is matched with handle j , and 0 otherwise

the HU value along the potential needle path. Let $T = \{t_1, t_2, \dots, t_m\}$ and $H = \{h_1, h_2, \dots, h_n\}$ denote the sets of detected needle tips and handles, respectively. The score O[i, j] for pairing tip t_i and handle h_j is defined as:

$$O[i,j] = \frac{\mu_{i,j}}{\sigma_{i,j}} \tag{15}$$

where $\mu_{i,j}$ and $\sigma_{i,j}$ denote the average and standard deviation of HU values on the line segment, respectively.

Constraints 8 and 9 ensure that each handle is matched with at most one tip and vice versa. Constraint 10 is formulated to regulate the length of the tip-handle pair which should be in close approximation to the pre-known needle length. Constraint 11 excludes the tip-handle pairs for which the detected angles at the tip and handle exhibit inconsistency. Constraint 12 ensures that no two needles intersect. While constraint 13 defines the binary nature of the decision variables, constraint 14 makes sure the total number of detected needles match the pre-known value.

3.3.2 The greedy matching and merging solving method

Several methods have been developed to solve the assignment problems. The Hungarian algorithm, designed for balanced problems, can be adapted for unbalanced ones by adding dummies, but struggles with complex constraints. Mathematical programming methods like integer and linear programming relaxation has advantage to find the optimality. However, in real-world complex problems, they face issues such as exponential computational complexity and difficulty in formulating complex constraints. Heuristic algorithms like genetic and greedy algorithms are useful alternatives. Genetic algorithms handle complex constraints well in large-scale problems, while greedy algorithms make fast, locally-optimal choices, providing practical solutions for real-world scenarios.

As for the above tip-handle matching UAP-C with complex constraints, we propose solving it using a greedy matching and merging strategy. Initially, a score matrix S, similar to that used in the Hungarian Method, is constructed to facilitate the pairing of tip-handle candidates. Each element of the score matrix S_{ij} is the score value of the potential needle path connecting the i-th tip and the j-th handle. To handle the specific constraints 10 and 11, we introduce a special

treatment when the corresponding value does not satisfy the prescribed criteria. In such cases, we assign the value of O[i,j] to negative infinity $(-\infty)$. This ensures that any pairings violating the geometric constraints are effectively excluded from the objective function, as they will no longer contribute to the selection process. By implementing this approach, we guarantee that only valid pairings that adhere to all the geometric restrictions are considered, thereby optimizing the overall matching solution.

An iterative greedy matching procedure is then applied to match all possible tip-handle pairs. At each iteration, the needle path with the highest score that does not intersect with any previously selected paths is chosen. This approach ensures that the non-intersection constraint is respected at every step. In the case of an $m \times n$ score matrix, applying the greedy matching process results in $x = \min(m, n)$ matching pairs between the m needle tips and n needle handles. Since the total number of implanted needles, denoted as N_{prior} , is known, if $x \leq N_{\text{prior}}$, the current matching solution set is accepted. However, if $x > N_{\text{prior}}$, this indicates the presence of duplicate needle paths and the following merging process is performed.

The merging process involves combining both the tip and handle of duplicate needle paths into a new, unified position. To identify duplicates, the algorithm first targets needle paths with lower score values. A low score typically suggests insufficient grayscale intensity along the path or poor intensity uniformity, which is often caused by duplicate paths that reduce the overall score. For needle paths with lower scores, if the tips and handles of two paths are within 2.5 mm of each other, they are classified as duplicates, and their respective tips and handles are merged. The merging process uses the masks of the tips and handles detected by our detection network. Specifically, for the tip (though the same procedure applies to the handle), when two duplicate tips are identified, the average non-zero Hounsfield Units (HU) within their respective detected mask regions are calculated. This average HU value is used as a weight to determine the new tip position, which is computed as the weighted sum of the two previous positions. This ensures that the new tip location reflects the weighted contribution of both original positions. The same procedure is applied to merge the handles of duplicate paths. The merging process is performed iteratively, refining the solution until the number of remaining needle paths is equal to $N_{\rm prior}$, the known target number of implanted needles.

4 Experiments and results

4.1 Patient data and preprocessing

One hundred intraoperative CT images were collected from colorectal cancer patients who had undergone SIBT. The study was approved by the Institutional Ethics Committee of Peking University Third Hospital (Beijing, China; Approval No.M2021438). The number of needles per image ranged from 2 to 43, with an average of 15.2 ± 8.2 . The CT images varied in resolution, with in-slice resolution ranging from $0.68\,\mathrm{mm}$ to $1.05\,\mathrm{mm}$ and slice thickness set at $5.0\,\mathrm{mm}$. The number of CT slices per image ranged from 7 to 29, with an average of 15.2 ± 5.4 . For the development of the detection method, the dataset was split into a training set and a test set at a ratio of 4:1.

Due to their finite size and the partial volume effect, the needle tip or handle may span multiple slices. Since a 2D network is used for tip-handle detection, all imaging areas of the handle or tip were annotated as the ground truth for training the detection network using ITK-SNAP software, in order to avoid misleading the network during learning. To validate the final matching results, the annotated 2D handles and tips were fused to obtain 3D positions, thereby determining the 3D needle paths. The 3D positions of the tip and handle were calculated as the intensity-weighted centroids of the annotated 2D handles and tips.

An image preprocessing step is applied to the CT scan to enhance the visibility of the needle paths, which facilitates the subsequent tip-handle matching process. This is achieved through the white top-hat transformation, a technique that highlights smaller, brighter structures, such as the needle paths, while suppressing larger background elements. The white top-hat transformation was implemented using the SimpleITK toolkit [49], applied slice-by-slice. A spherical structuring element with a radius of 5 pixels was used, which is sufficiently large relative to the size of the needle path, ensuring that the transformation effectively isolates the needle paths from surrounding tissues.

The performance of our proposed method was evaluated through a comparison with a segmentation-based baseline. In this baseline, the 3d-fullres nnUNet model [23] was applied to perform needle segmentation. To eliminate potential errors from automated separation, we manually separated any adjacent needles. Subsequently, we determined the 3D tip and handle locations by calculating the intensity-weighted centroids of manually annotated 2D handle and tip regions across the slices they spanned within the segmentation masks. The ground truth for the needle path mask was established through iterative pseudo-label generation and refinement, culminating in manual correction. Initially, we created pseudo-labels by generating a 3 mm-radius 3D cylindrical mask between the annotated needle tip and handle. These served to train the 3D-fullres nnUNet model using its default settings, which produced more precise labels. We repeated this process twice, applying manual corrections in the final iteration to obtain the definitive ground truth.

4.2 Implementation Details

4.2.1 Network Training

The tip-handle detection Network was developed using PyTorch and trained on an NVIDIA RTX 3090 GPU. Data augmentation, including cropping, scaling, shifting, and horizontal/vertical flipping were randomly performed to improve the stability of the training and the generalization ability of the model. The weight parameters for the loss functions λ_{HM} , λ_{off} and λ_{ang} are set to 2, 1 and 1, respectively.

For heatmap generation and heatmap loss, we empirically set the standard deviation of the Gaussian kernel $\sigma = \text{radius}/3$, $\alpha = 2$ and $\beta = 4$ in our experiments following the setting of previous works [28, 44]. Specifically, we set the radius as 4 mm for the needle handle and 3 mm for the needle tip.

To enhance the contrast of the needle tip and handle, the Hounsfield Unit (HU) values were thresholded at 800 (with all values exceeding 800 HU clamped to this upper limit) and linearly normalized to the [-1, 1] interval.

4.2.2 Evaluation metrics

To evaluate the proposed approach, a five-fold cross-validation was conducted. The 100 patients were randomly divided into five groups, each containing twenty patients. In each validation fold, four groups of patients were used to train the detection network, and the remaining group was used to validate tip-handle detection and matching. The evaluation framework includes both the 2D detection of needle tips and handles and the subsequent 3D localization of needles.

To quantitatively evaluate the 2D detection network for needle tips and handles, five metrics were employed: mean absolute error (MAE $_{\rm pos2d}$ in mm), angle error for tips and handles (MAE $_{\rm agl2d}$ in °), recall, precision, and F1 score. Manual annotations served as the ground truth. A detection was considered correct if the center distance between the predicted and ground truth positions was within 2 mm and the angle difference was within 5°.

The localization error, MAE_{pos2d} , was calculated as the average absolute distance between the 2D predicted position (\hat{p}_i) and the 2D ground truth position (p_i) across all tips or handles:

$$MAE_{pos2d} = \frac{1}{n} \sum_{i=1}^{n} |\hat{p}_i - p_i|$$
 (16)

The angular error for the needle tip or handle was calculated by averaging the absolute differences between the predicted $(\hat{\theta}_i)$ and ground truth angles

$$MAE_{agl2d} = \frac{1}{n} \sum_{i=1}^{n} \left| \hat{\theta}_i - \theta_i \right| \tag{17}$$

Here, n denotes the number of detected tips or handles.

Similarly, five metrics were employed to evaluate the performance of 3D needle localization. Firstly, standard detection evaluation metrics including precision, recall, and F1 score were utilized to assess the performance of the proposed method. A successful needle detection was defined as follows: the Euclidean distances between both the detected needle tip and handle positions and their corresponding ground truth positions must be within $2.5\,\mathrm{mm}$, and this detected needle must represent the closest match to the ground truth. The $2.5\,\mathrm{mm}$ threshold was set according to the slice thickness $(5\,\mathrm{mm})$ of the dataset.

Secondly, for the correctly detected needles, the localization accuracies for the tip-handle position and needle orientation were evaluated. The location accuracy of the tip and handle position using the MAE of the 3D position $(MAE_{tip3d}$ and $MAE_{hdl3d})$ and the relative error in each axis $(MAE_{tip-relx}, MAE_{tip-rely}, MAE_{tip-relz}, MAE_{hld-relx}, MAE_{hld-relx})$ to give a more thorough assess of the location accuracy. Let $\hat{P}_i = \{\hat{P}_{i,x}, \hat{P}_{i,y}, \hat{P}_{i,z}\} \in \mathbb{R}^3$ represent the ground truth position of the needle tip or handle for the i-th instance, $P_i = \{P_{i,x}, P_{i,y}, P_{i,z}\} \in \mathbb{R}^3$ represent the detected position of the needle tip for the same instance and n be the number of matched needles. With $\{s_x, s_y, s_z\}$ representing the spacing of the CT, the MAE_{tip3d} and MAE_{tip-x} were calculated as:

$$MAE_{tip3d} = \frac{1}{n} \sum_{i=1}^{n} \left| \hat{P}_i - P_i \right|$$
 (18)

$$MAE_{tip-relx} = \frac{1}{n} \sum_{i=1}^{n} \frac{\left| \hat{P}_{i,x} - P_{i,x} \right|}{s_x}$$

$$\tag{19}$$

Table 2: Detection results of needle handles and needle tips.

Object	MAE_{pos2d} (mm)	MAE_{agl2d} (°)	Recall	Precision	F1
Tip	1.25 ± 0.33	3.75 ± 2.10	99.4 ± 1.7	91.4 ± 8.3	95.0 ± 4.7
Handle	1.46 ± 0.61	2.12 ± 0.76	99.0 ± 2.0	93.1 ± 7.7	95.8 ± 4.6

The other MAEs were calculated similarly.

The localization accuracy of the needle orientation was evaluated via the error of the needle path angle, calculated as:

$$MAE_{agl3d} = \frac{1}{n} \sum_{i=1}^{n} \arccos\left(\hat{A}_i \cdot A_i\right)$$
 (20)

where A_i and \hat{A}_i denote the 3D orientation of the ground truth and detected needle.

4.3 Evaluation of needle tip and handle detection

Table 2 presents the quantitative results of detection network. From the results, it is evident that the needle handle exhibits more substantial positional deviations than the needle tip. In contrast, the needle handle's angular error is smaller than that of the needle tip. Given that the needle handle is larger than the needle tip, its greater size tends to amplify positional inaccuracies, resulting in increased deviations, while simultaneously enhancing angular resolution by magnifying detectable shifts in orientation.

The recall values for both the needle tip and handle are exceptionally high, indicating that the network rarely misses a target. Precision is slightly lower than recall, primarily due to some interfering factors that lead to false positives during detection.

From Fig. 4, it can be observed that the detection network accurately identifies the positions and orientations of both the needle tips and handles. The predicted results (bottom row) closely align with the ground truth annotations (top row), demonstrating the network's reliability in localizing and orienting the needles across different CT slices. Notably, in the last column, the network successfully detects a faint needle handle that was not annotated in the ground truth due to its subtle appearance, highlighting its sensitivity to challenging cases that are difficult to observe.

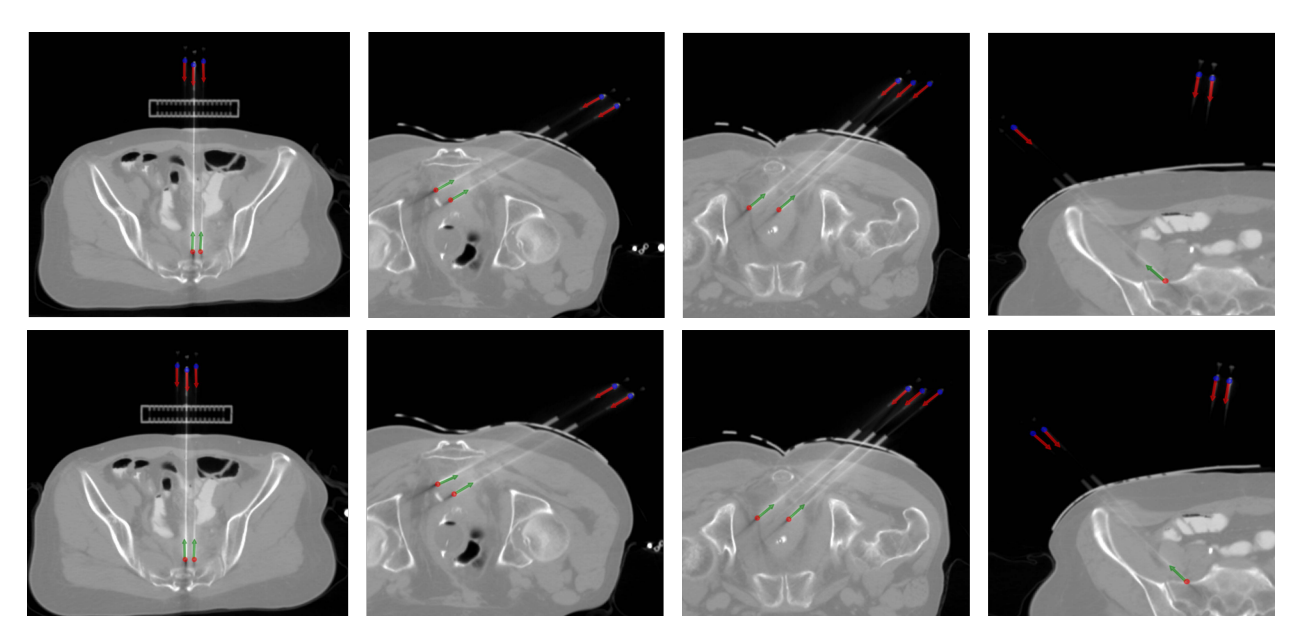


Figure 4: Qualitative results of the detection network. The upper row shows the ground truth annotations, and the lower row presents the predicted results for the corresponding CT slices. Blue and red dots indicate the positions of the needle tips and handles, respectively. Green and red arrows represent the directions of the needle tips and handles.

4.4 Evaluation of 3D needle localization

Table 3 compares the results of 3D needle detections between the proposed method and the segmentation-based method. Notably, the proposed method outperforms the segmentation-based method in terms of precision (92.7 ± 9.6 vs. 87.1 ± 8.7) and F1 score (90.3 ± 9.6 vs. 86.8 ± 8.7), with statistically significant *p*-values (< 0.01 and 0.03, respectively). The recall values are comparable between the two methods, with no significant difference (*p*-value = 0.13). These results indicate the presence of challenging cases where both methods fail; however, the proposed method demonstrates greater robustness against interference, resulting in fewer false positive needle detections.

As for the correctly detected needles, the proposed method demonstrates superior accuracy in localizing the needle tip. It achieves a lower $\text{MAE}_{\text{tip}3d}$ (1.05 \pm 0.36) compared to the segmentation-based method (1.34 \pm 0.51), and this difference is statistically significant (p-value = 0.02). The proposed method also shows lower errors in the x and z axes for tip localization ($\text{MAE}_{\text{tip-rel}x}$ and $\text{MAE}_{\text{tip-rel}z}$), with p-values of 0.07 and 0.04, respectively. Two methods have comparable performance in handle localization and path angle estimation. The values are similar between the two methods, and the p-values indicate no significant difference.

Table 3:	3D	needle	local	lization	result	S

Metric Method	Recall	Precision	F 1	$MAE_{tip3d} \\$	$MAE_{tip\text{-}relx}$	MAE _{tip-rely}
Segmentation-based	86.5 ± 9.1	87.1 ± 8.7	86.8 ± 8.7	1.34 ± 0.51	0.84 ± 0.41	0.78 ± 0.32
Proposed	88.6 ± 11.5	92.7 ± 9.6	90.3 ± 9.6	1.05 ± 0.36	0.64 ± 0.27	0.66 ± 0.20
p value	0.13	< 0.01	0.03	0.02	0.07	0.35

Metric Method	MAE _{tip-relz}	MAE _{hdl3d}	MAE _{hdl-relx}	MAE _{hdl-rely}	MAE _{hdl-relz}	MAE _{agl3d}
Segmentation-based	0.14 ± 0.10	1.61 ± 0.88	0.77 ± 0.44	1.18 ± 0.80	0.15 ± 0.13	0.30 ± 0.08
Proposed	0.10 ± 0.08	1.73 ± 0.95	0.75 ± 0.42	1.19 ± 0.87	0.16 ± 0.16	0.26 ± 0.06
p value	0.04	0.94	0.58	0.74	0.5	0.13

Note: The p value is calculated using a two-sided Wilcoxon signed-rank test.

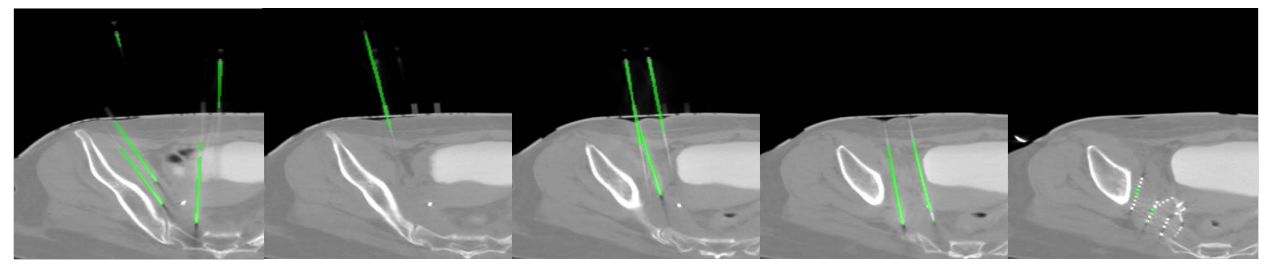
Fig.5 shows the segmentation and detection results on five consecutive slices for a patient case. Our method accurately identified all needles without any false positives or false negatives. However, the segmentation-based approach incorrectly detected the needle indicated by the yellow arrow, which spans three slices. This failure, consistent with the criteria discussed earlier, stems from a missing tip segmentation on the final slice due to seed interference. In contrast, our proposed tip-handle matching strategy demonstrates greater robustness and successfully detects this needle. Fig. 6 presents the 3D visualization of the detection result of the proposed method along with the iso-surface (-400) of the CT for three cases. While the needle visualization is somewhat unclear due to their subtle grayvalue distribution, the detected needles align well with the implanted needles, particularly evident around the needle guidance holes.

4.5 Computational efficiency

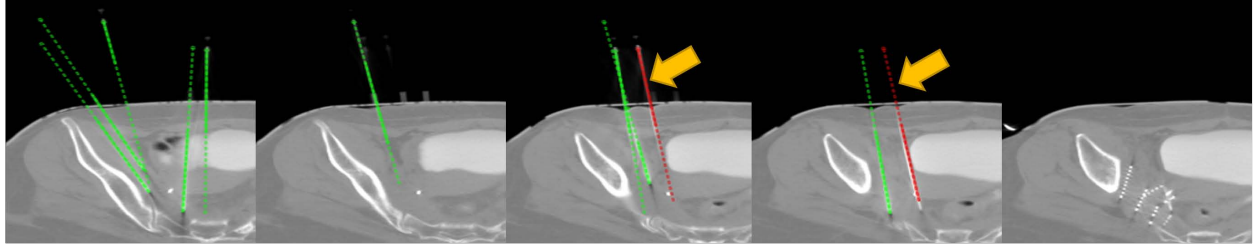
Processing time is a critical factor in clinical intraoperative planning. On a personal computer equipped with an Intel Xeon® Gold 5118 CPU and an NVIDIA RTX 3090 GPU, the computing time was 9.41 ± 8.95 seconds per case. The inference time for detecting the needle tip and handle was much quicker, at 1.83 ± 0.12 seconds, largely depending on the number of CT slices of the case. The majority of the computation time is spent on the matching process, which took an average of 7.57 ± 8.92 seconds. The time complexity of the proposed GMM algorithm is $O(n \log n)$, where n represents the number of needle tips or handles detected by the networks in this study. In the tested cases, the most extensive matching process involved 44 needles and took 24 seconds, while cases with 5 matched needles were processed in 0.34 seconds.

5 Discussion and conclusion

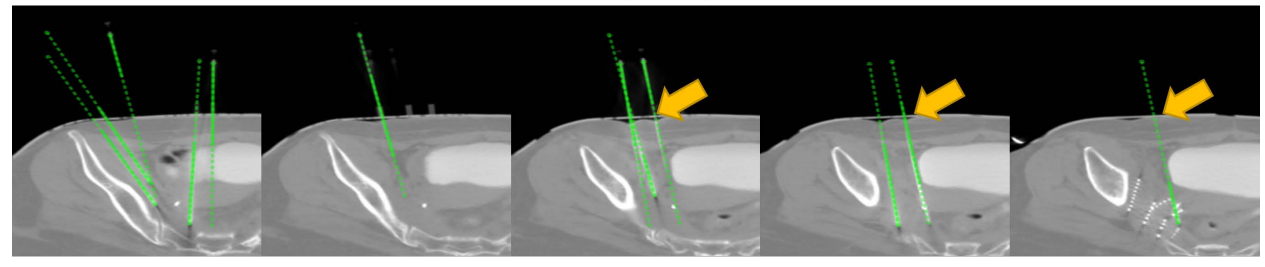
In this work, we developed a novel method to automatically localize needles in intraoperative CT for pelvic seed implant brachytherapy. In contrast to existing methods, this method novelly adopted a needle tip-handle detection and matching strategy, which was shown to be more effective to address the challenging imaging characteristics. The experimental results showed our method could achieve a 3D detection F1 score of 90.3 ± 9.6 , 3D tip-handle position



Segmentation result using nn-UNet



3D needle detection result using the segmentation-based method



3D needle detection result using the proposed method

Figure 5: Segmentation and detection results on five consecutive slices for a patient case. Correctly detected needles (True Positives) are marked in green, while incorrectly detected lines (False Positives) are in red. Solid lines indicate the portion of the needles intersecting the current image slice. Dotted lines represent parts of the correctly detected needles located on other slices.

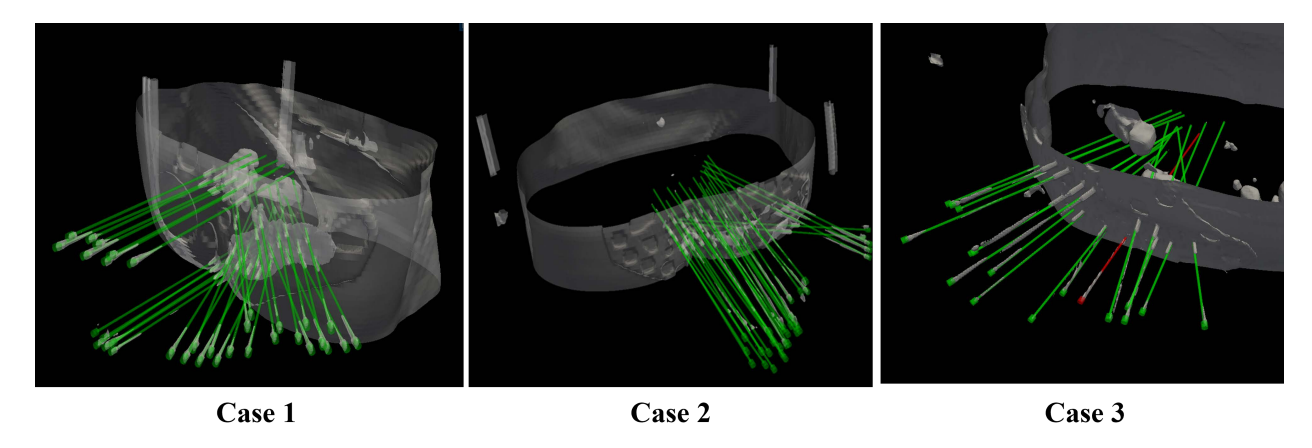


Figure 6: 3D visualization of the detected needles of the proposed method along with the iso-surface (-400) of the CT for three cases. Green lines represent correctly detected needles (TP), red lines indicate incorrectly detected needles (FP) and missed needles (FN).

MAE of $1.05\pm0.36\,\mathrm{mm}$ and $1.73\pm0.95\,\mathrm{mm}$, overall better than the existing most promising segmentation-based method. To the best of our knowledge, our proposed method is the first to employ a detection and matching framework for multi-needle localization.

For the compared segmentation-based method, we chose to utilize the nnUNet model instead of other segmentation methods. As a state-of-the-art, self-configuring framework for medical image segmentation, nnUNet provides a robust baseline by automatically optimizing network parameters for the dataset. This ensures a fairer comparison, focused on the merits of our proposed 3D localization and matching strategies, rather than being influenced by potential limitations of less specialized segmentation networks. Furthermore, to avoid uncertainty introduced by needle separation methods, we chose to manually extract individual needle paths. In this case, the results presented by our tests represent the best possible results obtainable from the segmentation, further emphasizing the advantage of our proposed method.

Although 3D detection may seem intuitive for the first step, 2D detection offers a more practical and efficient solution in our context. 3D detection methods typically demand a substantial dataset for effective training, and manually annotating the tip/handle 3D position for studied CTs is less efficient compared to 2D annotation. Acquiring large, annotated 3D CT datasets can be both challenging and expensive. Furthermore, even if 3D detection were employed, matching needle tips and handles would still be a necessary step to establish the complete 3D needle path.

For UAP-C, achieving a global optimum within an ideal timeframe is challenging due to its combinatorial nature and the complexity introduced by constraints. While exact methods, such as integer programming, can guarantee optimality, they are often computationally expensive, especially for large-scale problems. Therefore, heuristic and metaheuristic approaches offer practical alternatives for finding near-optimal solutions in a clinically acceptable timeframe. In this study, we adopted a GMM strategy to solve the UAP-C. While GMM does not guarantee optimality, it provides a balance between computational efficiency and solution quality. The effectiveness of this approach is supported by the strong performance observed in our five-fold cross-validation evaluation across 100 patient cases. In future work, we aim to investigate whether incorporating perturbation operators, such as variable neighborhood search, could further enhance the solution quality, given their promising results in other matching problem contexts [50].

CT-guided needle puncture encompasses a wide range of scenarios and anatomical sites, yet this study validates the proposed framework on pelvic images. The method demonstrates promising results for pelvic SIBT, and future work will focus on extending and adapting this framework to address the challenges of needle localization in other anatomical regions (e.g., head and neck, liver, lungs) and for other types of CT-guided interventions involving metal needles (e.g., electrode placement, microwave ablation). This will involve investigating modifications to the detection and matching algorithms to account for variations in image characteristics, anatomical complexity, and needle configurations, ultimately aiming to develop a robust and generalizable solution for automated needle localization across diverse clinical applications.

References

- [1] Freddie Bray, Mathieu Laversanne, Hyuna Sung, Jacques Ferlay, Rebecca L. Siegel, Isabelle Soerjomataram, and Ahmedin Jemal. Global cancer statistics 2022: GLOBOCAN estimates of incidence and mortality worldwide for 36 cancers in 185 countries. *CA: A Cancer Journal for Clinicians*, 74(3):229–263, May 2024.
- [2] Hao Wang, Hong-Bing Shi, Wei-Guang Qiang, Chao Wang, Bai Sun, Ye Yuan, and Wen-Wei Hu. CT-guided Radioactive 125I Seed Implantation for Abdominal Incision Metastases of Colorectal Cancer: Safety and Efficacy in 17 Patients. *Clinical Colorectal Cancer*, 22(1):136–142, March 2023.
- [3] Rafael Martínez-Monge, Subir Nag, and Edward W Martin. 125iodine brachytherapy for colorectal adenocarcinoma recurrent in the pelvis and paraortics. *International Journal of Radiation Oncology*Biology*Physics*, 42(3):545–550, October 1998.
- [4] Yuliang Jiang, Zhe Ji, Fuxin Guo, Ran Peng, Haitao Sun, Jinghong Fan, Shuhua Wei, Weiyan Li, Kai Liu, Jinghua Lei, and Junjie Wang. Side effects of CT-guided implantation of 125I seeds for recurrent malignant tumors of the head and neck assisted by 3D printing non co-planar template. *Radiation Oncology*, 13(1):18, December 2018.
- [5] Alfredo Polo, Carl Salembier, Jack Venselaar, and Peter Hoskin. Review of intraoperative imaging and planning techniques in permanent seed prostate brachytherapy. *Radiotherapy and Oncology*, 94(1):12–23, January 2010.
- [6] Subir Nag, Jay P Ciezki, Robert Cormack, Stephen Doggett, Keith DeWyngaert, Gregory K Edmundson, Richard G Stock, Nelson N Stone, Yan Yu, and Michael J Zelefsky. Intraoperative planning and evaluation of permanent prostate brachytherapy: Report of the American Brachytherapy Society. *International Journal of Radiation Oncology*Biology*Physics*, 51(5):1422–1430, December 2001.
- [7] Alireza Mehrtash, Mohsen Ghafoorian, Guillaume Pernelle, Alireza Ziaei, Friso G. Heslinga, Kemal Tuncali, Andriy Fedorov, Ron Kikinis, Clare M. Tempany, William M. Wells, Purang Abolmaesumi, and Tina Kapur. Automatic Needle Segmentation and Localization in MRI With 3-D Convolutional Neural Networks: Application to MRI-Targeted Prostate Biopsy. *IEEE Transactions on Medical Imaging*, 38(4):1026–1036, April 2019.

- [8] Hyunuk Jung, Chenyang Shen, Yesenia Gonzalez, Kevin Albuquerque, and Xun Jia. Deep-learning assisted automatic digitization of interstitial needles in 3D CT image based high dose-rate brachytherapy of gynecological cancer. *Physics in Medicine & Biology*, 64(21):215003, October 2019.
- [9] Yupei Zhang, Xiuxiu He, Zhen Tian, Jiwoong Jason Jeong, Yang Lei, Tonghe Wang, Qiulan Zeng, Ashesh B. Jani, Walter J. Curran, Pretesh Patel, Tian Liu, and Xiaofeng Yang. Multi-Needle Detection in 3D Ultrasound Images Using Unsupervised Order-Graph Regularized Sparse Dictionary Learning. *IEEE Transactions on Medical Imaging*, 39(7):2302–2315, July 2020.
- [10] Yupei Zhang, Zhen Tian, Yang Lei, Tonghe Wang, Pretesh Patel, Ashesh B Jani, Walter J Curran, Tian Liu, and Xiaofeng Yang. Automatic multi-needle localization in ultrasound images using large margin mask RCNN for ultrasound-guided prostate brachytherapy. *Physics in Medicine & Biology*, 65(20):205003, October 2020.
- [11] Xianjin Dai, Yang Lei, Yupei Zhang, Richard L.J. Qiu, Tonghe Wang, Sean A. Dresser, Walter J. Curran, Pretesh Patel, Tian Liu, and Xiaofeng Yang. Automatic multi-catheter detection using deeply supervised convolutional neural network in MRI-guided HDR prostate brachytherapy. *Medical Physics*, 47(9):4115–4124, September 2020.
- [12] Christoffer Andersén, Tobias Rydén, Per Thunberg, and Jakob H. Lagerlöf. Deep learning-based digitization of prostate brachytherapy needles in ultrasound images. *Medical Physics*, 47(12):6414–6420, December 2020.
- [13] Amanda M. Aleong, Alejandro Berlin, Jette Borg, Joelle Helou, Akbar Beiki-Ardakani, Alexandra Rink, Srinivas Raman, Peter Chung, and Robert A. Weersink. Rapid multi-catheter segmentation for magnetic resonance image-guided catheter-based interventions. *Medical Physics*, 51(8):5361–5373, August 2024.
- [14] Amani Shaaer, Moti Paudel, Mackenzie Smith, Frances Tonolete, and Ananth Ravi. Deep-learning-assisted algorithm for catheter reconstruction during MR-only gynecological interstitial brachytherapy. *Journal of Applied Clinical Medical Physics*, 23(2):e13494, February 2022.
- [15] William Thomas Hrinivich, Douglas A. Hoover, Kathleen Surry, Chandima Edirisinghe, Jacques Montreuil, David D'Souza, Aaron Fenster, and Eugene Wong. Simultaneous automatic segmentation of multiple needles using 3D ultrasound for high-dose-rate prostate brachytherapy. *Medical Physics*, 44(4):1234–1245, April 2017.
- [16] Hua Zhou, Wu Qiu, Mingyue Ding, and Songgen Zhang. Automatic needle segmentation in 3D ultrasound images using 3D improved Hough transform. In Michael I. Miga and Kevin R. Cleary, editors, *Medical Imaging*, page 691821, San Diego, CA, March 2008.
- [17] Wenqi Zhou, Xinzhou Li, Fatemeh Zabihollahy, David S. Lu, and Holden H. Wu. Deep learning-based automatic pipeline for 3D needle localization on intra-procedural 3D MRI. *International Journal of Computer Assisted Radiology and Surgery*, 19(11):2227–2237, March 2024.
- [18] Charles R. Hatt, Gary Ng, and Vijay Parthasarathy. Enhanced needle localization in ultrasound using beam steering and learning-based segmentation. *Computerized Medical Imaging and Graphics*, 41:46–54, April 2015.
- [19] M. Barva, M. Uhercik, J.-M. Mari, J. Kybic, J.-R. Duhamel, H. Liebgott, V. Hlavac, and C. Cachard. Parallel integral projection transform for straight electrode localization in 3-D ultrasound images. *IEEE Transactions on Ultrasonics, Ferroelectrics and Frequency Control*, 55(7):1559–1569, July 2008.
- [20] Yongnan Zheng, Shan Jiang, Zhiyong Yang, and Lin Wei. Automatic needle detection using improved random sample consensus in CT image-guided lung interstitial brachytherapy. *Journal of Applied Clinical Medical Physics*, 22(4):121–131, April 2021.
- [21] Nobuyuki Otsu. A Threshold Selection Method from Gray-Level Histograms. *IEEE Transactions on Systems, Man, and Cybernetics*, 9(1):62–66, January 1979.
- [22] Olaf Ronneberger, Philipp Fischer, and Thomas Brox. U-Net: Convolutional Networks for Biomedical Image Segmentation, May 2015.
- [23] Fabian Isensee, Paul F. Jaeger, Simon A. A. Kohl, Jens Petersen, and Klaus H. Maier-Hein. nnU-Net: A self-configuring method for deep learning-based biomedical image segmentation. *Nature Methods*, 18(2):203–211, February 2021.
- [24] Julia F. Barrett and Nicholas Keat. Artifacts in CT: Recognition and Avoidance. *RadioGraphics*, 24(6):1679–1691, November 2004.
- [25] Zhengxia Zou, Keyan Chen, Zhenwei Shi, Yuhong Guo, and Jieping Ye. Object Detection in 20 Years: A Survey. *Proceedings of the IEEE*, 111(3):257–276, March 2023.
- [26] Shaoqing Ren, Kaiming He, Ross Girshick, and Jian Sun. Faster R-CNN: Towards Real-Time Object Detection with Region Proposal Networks. *IEEE Transactions on Pattern Analysis and Machine Intelligence*, 39(6):1137–1149, June 2017.

- [27] Joseph Redmon, Santosh Divvala, Ross Girshick, and Ali Farhadi. You Only Look Once: Unified, Real-Time Object Detection. In 2016 IEEE Conference on Computer Vision and Pattern Recognition (CVPR), pages 779–788, Las Vegas, NV, USA, June 2016. IEEE.
- [28] Hei Law and Jia Deng. Cornernet: Detecting objects as paired keypoints. In *Proceedings of the European conference on computer vision (ECCV)*, pages 734–750, 2018.
- [29] Kaiwen Duan, Song Bai, Lingxi Xie, Honggang Qi, Qingming Huang, and Qi Tian. CenterNet: Keypoint Triplets for Object Detection. In 2019 IEEE/CVF International Conference on Computer Vision (ICCV), pages 6568–6577, Seoul, Korea (South), October 2019. IEEE.
- [30] Wei Liu, Dragomir Anguelov, Dumitru Erhan, Christian Szegedy, Scott Reed, Cheng-Yang Fu, and Alexander C. Berg. SSD: Single Shot MultiBox Detector. volume 9905, pages 21–37. 2016.
- [31] Nicolas Carion, Francisco Massa, Gabriel Synnaeve, Nicolas Usunier, Alexander Kirillov, and Sergey Zagoruyko. End-to-End Object Detection with Transformers, May 2020.
- [32] H. W. Kuhn. The Hungarian method for the assignment problem. *Naval Research Logistics Quarterly*, 2(1-2):83–97, March 1955.
- [33] Athanasios K. Ziliaskopoulos. A Linear Programming Model for the Single Destination System Optimum Dynamic Traffic Assignment Problem. *Transportation Science*, 34(1):37–49, February 2000.
- [34] Vittorio Maniezzo, Marco Antonio Boschetti, and Thomas Stützle. *Matheuristics: Algorithms and Implementations*. EURO Advanced Tutorials on Operational Research. Springer International Publishing, Cham, 2021.
- [35] Joseph B. Mazzola. Generalized Assignment with Nonlinear Capacity Interaction. *Management Science*, 35(8):923–941, August 1989.
- [36] Anshuman Sahu and Rudrajit Tapadar. Solving the Assignment problem using Genetic Algorithm and Simulated Annealing.
- [37] Andrea Galadíková and Branislav Časnocha. Using simulated annealing for personnel assignment in railway nodes. In 2024 IEEE 17th International Scientific Conference on Informatics (Informatics), pages 69–74, Poprad, Slovakia, November 2024. IEEE.
- [38] Alexander Kinast, Roland Braune, Karl F. Doerner, Stefanie Rinderle-Ma, and Christian Weckenborg. A hybrid metaheuristic solution approach for the cobot assignment and job shop scheduling problem. *Journal of Industrial Information Integration*, 28:100350, July 2022.
- [39] Fabian Schäfer, Manuel Walther, Dominik G. Grimm, and Alexander Hübner. Combining machine learning and optimization for the operational patient-bed assignment problem. *Health Care Management Science*, 26(4):785–806, December 2023.
- [40] Sascha Hamzehi, Klaus Bogenberger, Philipp Franeck, and Bernd Kaltenhauser. Combinatorial Reinforcement Learning of Linear Assignment Problems. In 2019 IEEE Intelligent Transportation Systems Conference (ITSC), pages 3314–3321, Auckland, New Zealand, October 2019. IEEE.
- [41] Alexander Kline, Darryl Ahner, and Raymond Hill. The Weapon-Target Assignment Problem. *Computers & Operations Research*, 105:226–236, May 2019.
- [42] Qinyun Zhu and Jae Oh. Deep Reinforcement Learning for Fairness in Distributed Robotic Multi-type Resource Allocation. In 2018 17th IEEE International Conference on Machine Learning and Applications (ICMLA), pages 460–466, Orlando, FL, December 2018. IEEE.
- [43] Ke Sun, Bin Xiao, Dong Liu, and Jingdong Wang. Deep High-Resolution Representation Learning for Human Pose Estimation. In 2019 IEEE/CVF Conference on Computer Vision and Pattern Recognition (CVPR), pages 5686–5696, Long Beach, CA, USA, June 2019. IEEE.
- [44] Xingyi Zhou, Dequan Wang, and Philipp Krähenbühl. Objects as points. arXiv preprint arXiv:1904.07850, 2019.
- [45] Ethan H. Nguyen, Haichun Yang, Ruining Deng, Yuzhe Lu, Zheyu Zhu, Joseph T. Roland, Le Lu, Bennett A. Landman, Agnes B. Fogo, and Yuankai Huo. Circle Representation for Medical Object Detection. *IEEE Transactions on Medical Imaging*, 41(3):746–754, March 2022.
- [46] Jifeng Dai, Haozhi Qi, Yuwen Xiong, Yi Li, Guodong Zhang, Han Hu, and Yichen Wei. Deformable convolutional networks. In *Proceedings of the IEEE international conference on computer vision*, pages 764–773, 2017.
- [47] Tsung-Yi Lin, Priya Goyal, Ross Girshick, Kaiming He, and Piotr Dollar. Focal Loss for Dense Object Detection. *IEEE Transactions on Pattern Analysis and Machine Intelligence*, 42(2):318–327, February 2020.

- [48] Xue Yang and Junchi Yan. Arbitrary-Oriented Object Detection with Circular Smooth Label. In Andrea Vedaldi, Horst Bischof, Thomas Brox, and Jan-Michael Frahm, editors, *Computer Vision ECCV 2020*, volume 12353, pages 677–694. Springer International Publishing, Cham, 2020.
- [49] Bradley C. Lowekamp, David T. Chen, Luis Ibáñez, and Daniel Blezek. The Design of SimpleITK. Frontiers in Neuroinformatics, 7, 2013.
- [50] Harol Mauricio Gámez Albán, Trijntje Cornelissens, and Kenneth Sörensen. A new policy for scattered storage assignment to minimize picking travel distances. *European Journal of Operational Research*, 315(3):1006–1020, June 2024.